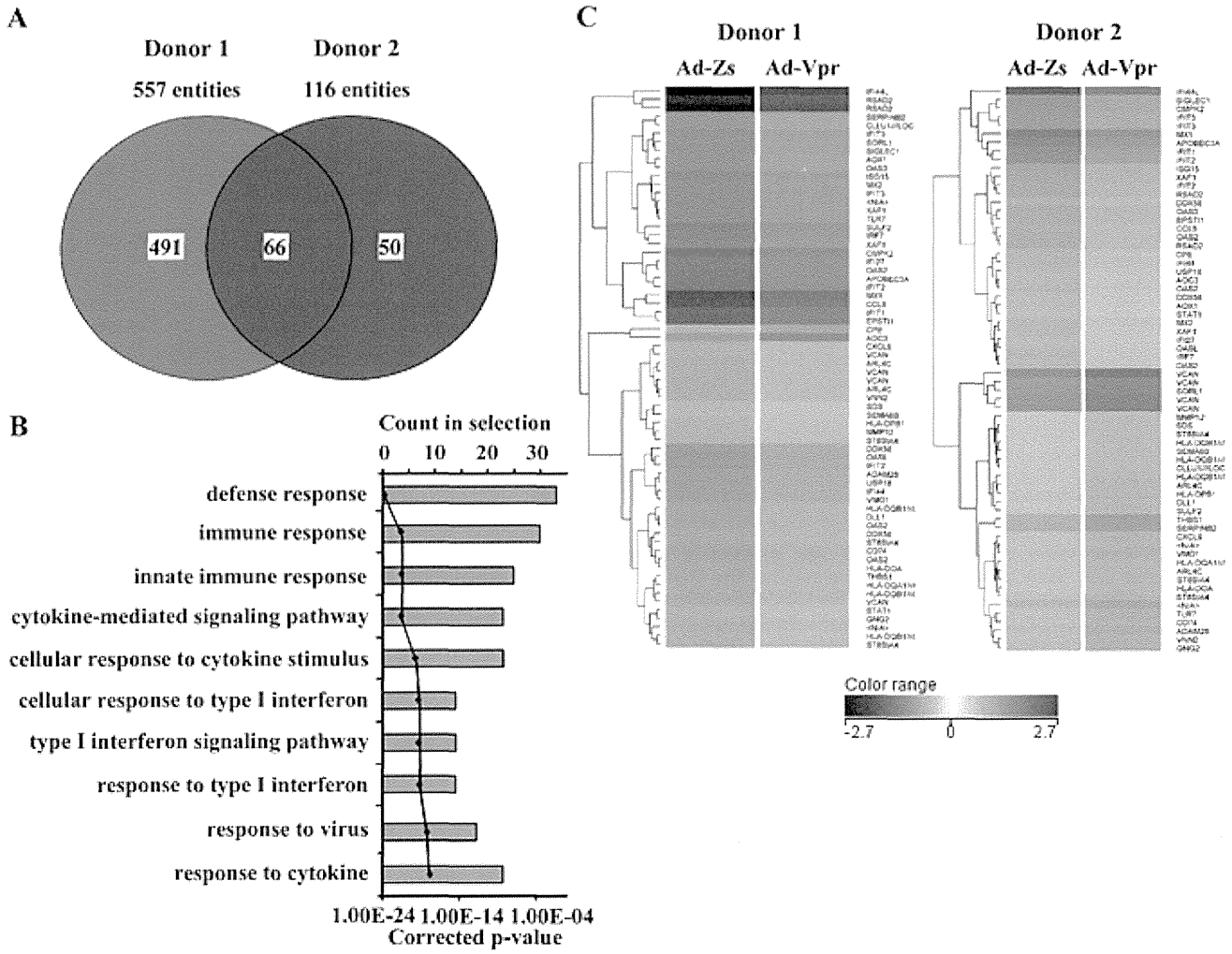

Figure 4. Gene ontology of differentially expressed genes after infection of human monocyte-derived macrophages (MDMs) with Ad-Vpr. (A) Venn diagram representing the number of differentially expressed cellular genes (>2-fold change in both donors) after infection of human MDMs with Ad-Vpr. (B) The top ten genes ontology classified by corrected p-value, and (C) heat map of hierarchical gene clustering of the 66 differentially regulated in both donors. Gene up-regulation is denoted in red and gene down-regulation is denoted in blue.
doi:10.1371/journal.pone.0106418.g004

common to both donors. The transcriptional levels of 15 genes were measured in Donor 1 by qRT-PCR with the primers listed in Table 2, using *GAPDH* as an internal control. In general, there was a strong correlation between the microarray data and the qRT-PCR data at 48 h post-infection; the two techniques yielded very similar expression profiles for all 15 genes in Donor 1 (Figure 6 and Table 1). However, there were some discrepancies, e.g., the qRT-PCR results showed a slightly higher increase than the microarray analysis for *IFI27*. Similarly, the expression levels of *IFIT1*, *IFI44L*, *MX1*, and *RSAD2* (which encodes the viperin protein) were higher in the microarray data compared to their respective relative expression levels in the qRT-PCR data. On the other hand, in Donor 2 except for *IRF7* (4-fold) and *MX1* (5-fold) higher expression levels of *APOBEC3A* (233-fold), *ISG20* (132-fold), *IFIT2* (97-fold), *IFIT1* (51-fold), *ISG15* (38-fold), *IFI27* (47-fold), *IFI44L* (36-fold), *TNFSF10* (*TRAIL*) (29-fold), *RSAD2* (22-fold), *MX2* (17-fold), *IFIT3* (16-fold), *DDX58* (12-fold) and *STAT1* (5-fold) were observed by qRT-PCR compared to their respective microarray data (Figure 6 and Table 1). These inconsistencies were probably due to the differences in transcripts variants or due to the intrinsic differences between the two techniques, notably in the normalization methods. For microarray experiments, the normalization was based on a large number of genes, whereas in the qRT-PCR experiments, a single housekeeping gene was used as an internal control against which the results were normalized. Overall, the qRT-PCR results were in agreement with the array data i.e. differential up-regulation giving us strong confidence in the interpretation of the gene expression data obtained through microarray.

Next, to demonstrate whether similar results could be obtained in other healthy donors, the transcriptional levels of these 15 genes were measured in MDMs derived from three additional healthy donors (Donors 3–5) by qRT-PCR. As shown in Figure 6, the expression profiles of the three additional donors were generally consistent with the data obtained from Donor 1. However, the expression levels of the *IFI27* and *IFI44L* genes, which were up-regulated approximately 7-fold and 40-fold, respectively, in the presence of Vpr in MDMs derived from Donor 1, were only slightly up-regulated in Donors 3 and 4. These results indicated that the activation of the type I IFN pathway was common to all the tested healthy donors.

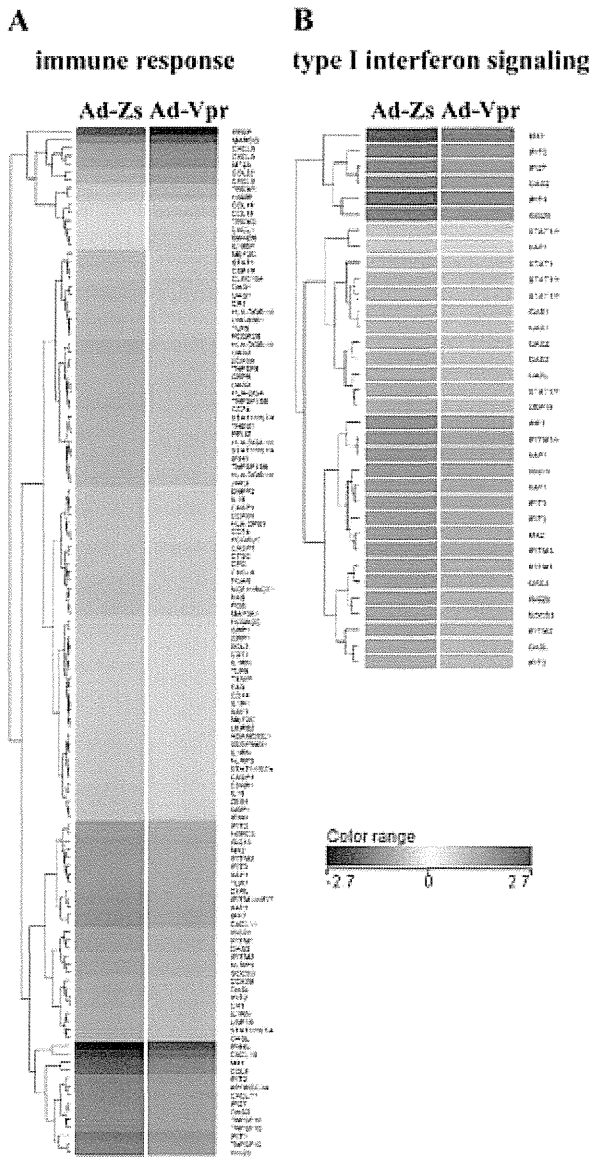

Figure 5. Differential expression profiling of cellular genes involved in the immune response and the type I interferon pathway after infection with Ad-Vpr in human monocyte-derived macrophages (MDMs) from Donor 1. Heat map showing genes related to the immune response (left: GO: 0006955) and the type I interferon signaling (right: GO: 0060337) that were either up- or down-regulated (>2-fold change) upon Ad-Vpr infection of MDMs from Donor 1. The color coding represents the normalized expression of genes in MDMs infected with Ad-Vpr or Ad-Zs (see color key). Gene up-regulation is denoted in red and gene down-regulation is denoted in blue.

doi:10.1371/journal.pone.0106418.g005

Confirmation of protein expression by Western blotting

Finally, Western blotting was performed to examine the effect of HIV-1 Vpr on the protein expression levels of IRF7, STAT1, ISG15, ISG20, APOBEC3A, and TRAIL in MDMs. Cell lysates were prepared from Ad-Vpr, Ad-Zs, or mock-infected MDMs and subjected to Western blotting using specific antibodies. β-actin was used as a loading control. Consistent with the microarray data and the qRT-PCR results, STAT1, ISG15, ISG20, IRF7, and TRAIL were up-regulated in Ad-Vpr-infected macrophages compared to Ad-Zs- or mock-infected controls (Figure 7); however, APOBEC3A, which was originally shown to be up-regulated at the transcriptional level by both microarray and real-time PCR, was not induced at the protein level compared to controls, as measured by Western blotting (Figure 7). Why the *APOBEC3A* gene transcript failed to express its gene product is not clear; however, differential regulation of gene transcription does not ensure a corresponding change in gene product levels. Taken together, these results clearly indicate that HIV-1 Vpr protein leads to the activation of the type I IFN pathway and the subsequent up-regulation of various ISGs in human MDMs.

Discussion

The data presented herein are the first analysis of the changes in gene transcription that occur following *in vitro* infection of human MDMs with an adenovirus expressing HIV-1 Vpr protein. Although some previous studies have shown that HIV-1 infection leads to the activation of innate immunity and thus the induction of various ISGs in human MDMs [5,29–37], the specific role of Vpr in the induction of ISGs in human MDMs has not been documented.

In this study, by utilizing an Affymetrix oligonucleotide microarray, we demonstrated that the majority of the genes differentially regulated by Ad-Vpr in both donors were involved in the immune response, indicating the important role played by HIV-1 Vpr protein in human MDMs. A large number of genes from this group is predicted to be activated during the innate immune response (Table 1) as part of the host defense response to clear viral infections [27,28,38]. We observed an increase in the levels of various ISGs such as *MX1, IFI44L, DDX58, RSAD2*, and several of the *IFITs*, which have been shown to play an important role against HIV-1 infection in MDMs [31]. MX2 has recently been reported to be an IFN-induced inhibitor of HIV-1 infection in human monocytoid cell lines [39]. Since the differential expression levels of the *MX1, MX2, IFIT1, IFIT2, IFIT3, IFIT27, IFI44L, DDX58*, and *RSAD2* genes obtained through microarray strongly correlated with the real-time PCR data, it is reasonable to speculate that the expression of these proteins may be up-regulated following HIV-1 infection in human MDMs.

Real-time PCR data and Western blot analysis confirmed the activation of IRF7 by HIV-1 Vpr in human MDMs (Figures 6 and 7). IRF7 is the master regulator of type I IFN-dependent immune responses [40] and plays an important role in HIV-1 pathogenesis [34]. IRF7 promotes autocrine and paracrine activation of STAT1 and plays a critical role in virus-mediated induction of IFN-α [41]. It is known that type I IFNs activate the Janus kinases (JAKs) and the STAT transcription factors, which ultimately leads to the expression of target genes [42,43]. The *STAT1* gene encodes a 91-kDa protein which is activated by both type I and type II IFNs [44]. This important transcription factor is phosphorylated by the JAKs in response to proinflammatory and regulatory factors [38]. It has been shown that the STAT1 pathway plays an important role in the pathogenesis of HIV-1 infection [45,46]; indeed, activation of the STAT1 pathway by HIV-1 Vpr is demonstrated in this study. We further showed that in the presence of Vpr protein the level of STAT1 phosphorylation at tyrosine 701 is much higher than the control recombinant adenovirus (Figure 7). The exact mechanism through which Vpr leads to the phosphorylation of STAT1 at tyrosine 701 is not known and requires further study.

HIV-1 Vpr protein caused the up-regulation of various ISGs, such as ISG15 and ISG20 (Figures 6 and 7), which can inhibit

Table 1. Differentially expressed genes (fold change >2.0) associated with immune response (GO: 0006955) upon Ad-Vpr infection in Donor 1 and Donor 2.

Probe Set ID	Gene Symbol	Entrez Gene	Fold Change		Regulation
			Donor 1	Donor 2	
214146_s_at	PPBP	5473	−96.30		Down
205819_at	MARCO	8685	−12.69		Down
215101_s_at	CXCL5	6374	−6.77		Down
207852_at	CXCL5	6374	−5.81		Down
212185_x_at	MT2A	4502	−6.16		Down
207861_at	CCL22	6367	−4.06		Down
214974_x_at	CXCL5	6374	−4.23		Down
219434_at	TREM1	54210	−2.61		Down
220491_at	HAMP	57817	−2.66		Down
209924_at	CCL18	6362	−2.15		Down
32128_at	CCL18	6362	−2.17		Down
219725_at	TREM2	54209	−2.01		Down
204470_at	CXCL1	2919	−2.10		Down
207069_s_at	SMAD6	4091	−2.07		Down
222868_s_at	IL18BP	10068	−2.07		Down
209200_at	MEF2C	4208	2.52		Up
209969_s_at	STAT1	6772	2.59	2.03	Up
203104_at	CSF1R	1436	2.54		Up
206682_at	CLEC10A	10462	2.56		Up
202869_at	OAS1	4938	2.75		Up
205552_s_at	OAS1	4938	2.75		Up
217552_x_at	CR1	1378	2.63		Up
211656_x_at	HLA-DQB1	3119	2.68	−2.06	Up/down
225869_s_at	UNC93B1	81622	2.70		Up
210166_at	TLR5	7100	2.70		Up
210889_s_at	FCGR2B	2213	2.70		Up
212998_x_at	HLA-DQB1	3119	3.12	−2.14	Up/down
228607_at	OAS2	4939	3.10	2.15	Up
222793_at	DDX58	23586	2.96	2.09	Up
235735_at	TNFSF8	944	2.97		Up
238581_at	GBP5	115362	3.00		Up
206553_at	OAS2	4939	3.01	2.24	Up
226878_at	HLA-DOA	3111	3.01	−2.37	Up
223502_s_at	TNFSF13B	10673	3.03		Up
1567628_at	CD74	972	3.04	−2.54	Up/down
M97935_MA_at	STAT1	6772	2.88		Up
201110_s_at	THBS1	7057	2.86	−3.44	Up/down
219132_at	PELI2	57161	2.86		Up
212671_s_at	HLA-DQA1	3117	2.84	−2.40	Up
M97935_MB_at	STAT1	6772	2.84		Up
1555464_at	IFIH1	64135	2.84		Up
223501_at	TNFSF13B	10673	2.80		Up
209823_x_at	HLA-DQB1	3119	2.82	−2.07	Up/down
227677_at	JAK3	3718	2.82		Up
209392_at	ENPP2	5168	2.32		Up
205992_s_at	IL15	3600	2.31		Up
211367_s_at	CASP1	834	2.31		Up
218986_s_at	DDX60	55601	2.31		Up

Table 1. Cont.

Probe Set ID	Gene Symbol	Entrez Gene	Fold Change		Regulation
			Donor 1	Donor 2	
244485_at	HLA-DPB1	3115	2.25	−2.19	Up
209619_at	CD74	972	2.28		Up
211395_x_at	FCGR2C	9103	2.28		Up
206011_at	CASP1	834	2.36		Up
231234_at	CTSC	1075	2.38		Up
205382_s_at	CFD	1675	2.40		Up
203915_at	CXCL9	4283	2.43	−2.44	Up/down
207674_at	FCAR	2204	2.42		Up
204961_s_at	NCF1	653361	2.44		Up
215719_x_at	FAS	355	2.44		Up
209189_at	FOS	2353	2.45		Up
214786_at	MAP3K1	4214	2.45		Up
210992_x_at	FCGR2C	9103	2.07		Up
231577_s_at	GBP1	2633	2.09		Up
202269_x_at	GBP1	2633	2.03		Up
204908_s_at	BCL3	602	2.04		Up
210140_at	CST7	8530	2.04		Up
216243_s_at	IL1RN	3557	2.04		Up
220832_at	TLR8	51311	2.05		Up
201008_s_at	TXNIP	10628	2.03		Up
216252_x_at	FAS	355	2.02		Up
201743_at	CD14	929	2.02		Up
202948_at	IL1R1	3554	2.01		Up
242234_at	XAF1	54739	2.01		Up
209199_s_at	MEF2C	4208	2.01		Up
210146_x_at	LILRB2	10288	2.01		Up
206134_at	ADAMDEC1	27299	2.12		Up
200986_at	SERPING1	710	2.13		Up
212659_s_at	IL1RN	3557	2.13		Up
216015_s_at	NLRP3	114548	2.15		Up
M97935_3_at	STAT1	6772	2.14		Up
211368_s_at	CASP1	834	2.15		Up
209906_at	C3AR1	719	2.18		Up
217371_s_at	IL15	3600	2.20		Up
212764_at	ZEB1	6935	2.23		Up
202270_at	GBP1	2633	2.22		Up
219209_at	IFIH1	64135	2.22		Up
204747_at	IFIT3	3437	4.73	3.70	Up
219863_at	HERC5	51191	4.71		Up
205483_s_at	ISG15	9636	5.16	3.16	Up
204994_at	MX2	4600	4.88	2.20	Up
212203_x_at	IFITM3	10410	4.93		Up
229450_at	IFIT3	3437	5.05	3.70	Up
206133_at	XAF1	54739	4.99	2.19	Up
220146_at	TLR7	51284	5.00	−2.58	Up/down
218983_at	C1RL	51279	5.32		Up
201601_x_at	IFITM1	10581	5.46		Up
228617_at	XAF1	54739	5.44	3.02	Up

Table 1. Cont.

Probe Set ID	Gene Symbol	Entrez Gene	Fold Change		Regulation
			Donor 1	Donor 2	
208436_s_at	IRF7	3665	5.87	2.16	Up
210163_at	CXCL11	6373	5.89		Up
33304_at	ISG20	3669	4.29		Up
214022_s_at	IFITM1	8519	4.46		Up
218400_at	OAS3	4940	4.41	2.82	Up
201315_x_at	IFITM2	10581	3.97		Up
207075_at	NLRP3	114548	4.09		Up
227697_at	SOCS3	9021	4.17		Up
218943_s_at	DDX58	23586	3.49	2.54	Up
205660_at	OASL	8638	3.65	2.13	Up
217502_at	IFIT2	3433	3.59	2.93	Up
244313_at	CR1	1378	3.59		Up
216244_at	IL1RN	3557	3.36		Up
219211_at	USP18	11274	3.32	2.26	Up
M97935_5_at	STAT1	6772	3.28		Up
210797_s_at	OASL	8638	3.23		Up
204439_at	IFI44L	10964	40.44	11.7	Up
204533_at	CXCL10	3627	22.91		Up
202086_at	MX1	4599	14.65	7.07	Up
214038_at	CCL8	6355	12.93	2.68	Up
226757_at	IFIT2	3433	7.64	4.52	Up
210873_x_at	APOBEC3A	200315	7.49	5.67	Up
211122_s_at	CXCL11	6373	7.45		Up
202411_at	IFI27	3429	7.03	2.14	Up
204972_at	OAS2	4939	7.05	2.72	Up
202687_s_at	TNFSF10	8743	6.85		Up
214329_x_at	TNFSF10	8743	6.95		Up
203153_at	IFIT1	3434	10.06	4.89	Up
202688_at	TNFSF10	8743	8.34		Up
204698_at	ISG20	3669	8.42		Up
216598_s_at	CCL2	6347		2.16	Up
236203_at	HLA-DQA	100507718		−3.46	Down
213831_at	HLA-DQA	100507718		−2.12	Down
209480_at	HLADQB	3119		−2.03	Down
209774_at	CXCL2	2920		−2.06	Down
211743_s_at	PRG2	5553		−2.40	Down
206978_at	CCR2	729230		−2.19	Down

doi:10.1371/journal.pone.0106418.t001

virus replication through different mechanisms [27,28]. Previously, it has been shown that HIV-1 Vpr protein activates NF-κB [47], which might explain the up-regulation of various ISGs in our study. The ISGs act through a variety of mechanisms to render cells resistant to viral infection [27]. It has been shown that ISG15 is induced in HIV-1-infected MDMs [27], where it restricts and impedes HIV-1 replication by causing ISGylation of viral Gag protein and certain cellular factors [33]. Similarly, ISG20 has been shown to exhibit antiviral activity against HIV-1 [48]. Induction and activation of ISGs such as ISG15, ISG20, the IFITs, and viperin are thought to be the reason MDMs are relatively resistant to cell death and can act as long-term carriers of HIV-1 [31]. The observation that these genes were up-regulated in Ad-Vpr-infected MDMs in our study suggests that in HIV-1-infected macrophages, Vpr is responsible for the induction of these ISGs; thus due to these ISGs, macrophages are relatively resistant to Vpr-induced cell death.

TRAIL protein is produced after HIV-1 infection in monocytes due to the IFNα/β-mediated activation of the STAT1 signaling cascade [49], and has been shown to cause apoptosis in several cell lines during HIV-1 infection. Although an initial increase in TRAIL protein was shown to kill HIV-1-infected macrophages

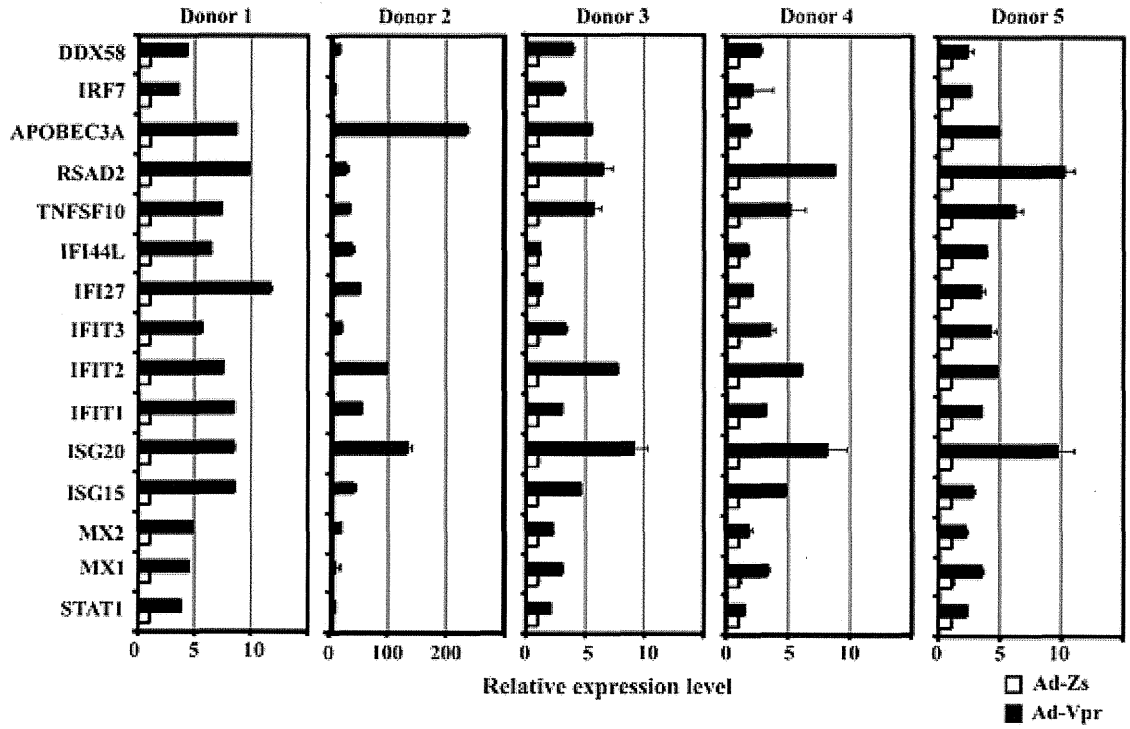

Figure 6. Validation of microarray data by qRT-PCR. Peripheral blood mononuclear cells (PBMCs) isolated from Donor 1, Donor 2 and three other healthy donors (Donors 3–5) through leukophoresis were cultured *in vitro* and differentiated into human MDMs as described in Materials and Methods. At day 7, the MDMs were infected with Ad-Vpr or Ad-Zs. At 48 h post-infection, RNA was extracted and subjected to qRT-PCR to amplify the selected genes using specific primers. Relative mRNA levels of the indicated genes are shown. Values are expressed as the fold change in Ad-Vpr-infected cells compared to Ad-Zs-infected cells and normalized to the expression of a housekeeping gene (*GAPDH*). The results represent the mean ± standard deviation (SD) of three samples from one experiment ($P<0.05$).
doi:10.1371/journal.pone.0106418.g006

[50], the exact role of TRAIL-mediated apoptosis in the elimination of HIV-1-infected cells is not known. Here, we have shown that HIV-1 Vpr protein caused elevated levels of TRAIL protein in macrophages (Figures 6 and 7), which would presumably help to eliminate HIV-1-infected cells through TRAIL-mediated cell death [29,50–52].

Table 2. Primers used for real-time PCR.

Name	5′ Sequence	3′ Sequence
STAT1	CCATCCTTTGGTACAACATGC	TGCACATGGTGGAGTCAGG
MX1	CAGCACCTGATGGCCTATCA	ACGTCTGGAGCATGAAGAACTG
MX2	AAACTGTTCAGAGCACGATTGAAG	ACCATCTGCTCCATTCTGAACTG
ISG15	ACTCATCTTTGCCAGTACAGGAG	CAGCATCTTCACCGTCAGGTC
ISG20	TCACCCCTCAGCACATGGT	TTCAGGAGCTGCAGGATCTCTAG
IFIT1	GCAGCCAAGTTTTACCGAAG	GCCCTATCTGGTGATGCAGT
IFIT2	CGAACAGCTGAGAATTGCAC	CAAGTTCCAGGTGAAATGGC
IFIT3	AGTCTAGTCACTTGGGGAAAC	ATAAATCTGAGCATCTGAGAGTC
IFI27	GGCAGCCTTGTGGCTACTCT	ATGGAGCCCAGGATGAACTTG
IFI44L	GTATAGCATATGTGGCCTTGCTTACT	ATGACCCGGCTTTGAGAAGTC
TNFSF10	GAGCTGAAGCAGATGCAGGAC	TGACGGAGTTGCCACTTGACT
RSAD2	AGGTTCTGCAAAGTAGAGTTGC	GATCAGGCTTCCATTGCTC
APOBEC3A	GAGAAGGGACAAGCACATGG	GTCTTATGCCTTCCAATGCC
IRF7	TACCATCTACCTGGGCTTCG	AGGGTTCCAGCTTCACCA
DDX58	ATCCCAGTGTATGAACAGCAG	GCCTGTAACTCTATACCCATGTC
GAPDH	ACAGTCAGCCGCATCTTCTTTTGC	TTGAGGTCAATGAAGGGGTC

doi:10.1371/journal.pone.0106418.t002

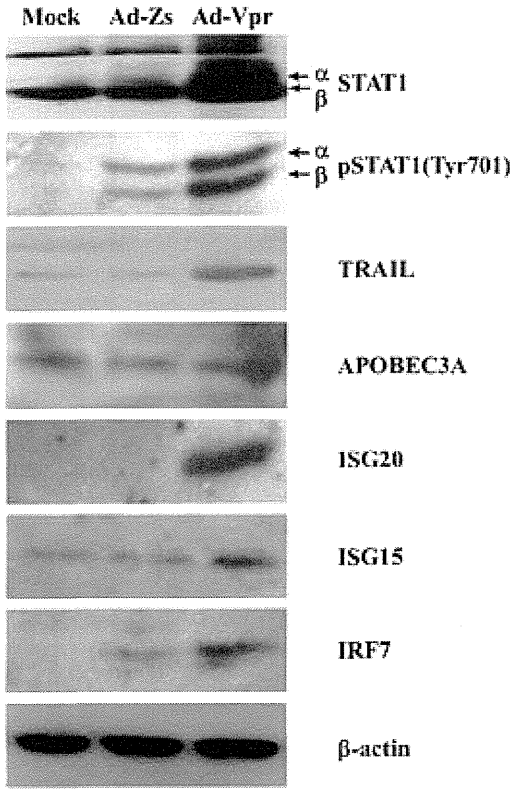

Figure 7. Validation of differentially expressed genes at the protein level. Human monocyte-derived macrophages (MDMs) were infected with Ad-Vpr or Ad-Zs, or mock-infected as a control. At 48 h post-infection, the cells were washed, lysed, and subjected to Western blot analyses with the indicated antibodies. A β-actin antibody was used as a loading control.
doi:10.1371/journal.pone.0106418.g007

Our findings further demonstrated that HV-1 Vpr differentially regulated the expression levels of chemotactic cytokines such as *CXCL1, CXCL5, CXCL7, CXCL9, CXCL10*, and *CXCL11* (Table 1). A previous report has shown that *CXCL10* and *CXCL11* are up-regulated in HIV-1-infected macrophages and play a key role in the recruitment and spread of HIV-1 to susceptible $CD4^+$ T-cells [53]. Surprisingly, our microarray data also showed that *CXCL10* and *CXCL11* were up-regulated in MDMs, by 23-fold and 7-fold, respectively (Table 1). Whether HIV-1 Vpr has a role in HIV-1 dissemination and the mechanism through which Vpr leads to the differential regulation of these chemokines in MDMs is not known. However, the recruitment of susceptible T-cells by HIV-1-infected human macrophages and the role of CXCL10 and CXCL11 will be intriguing to investigate in future studies.

HIV-1 Vpr is essential for efficient infection of non-dividing cells such as macrophages. It has been shown that HIV-1 Vpr is expressed within infected cells and is packaged into HIV-1 virions. Although, the virion-associated Vpr is able to cause cell cycle arrest of $CD4^+$ T cells in vivo [54], the induction of ISGs by this biologically active form of Vpr is not known. However, our recent studies have confirmed that the induction of ISGs in HIV-1_{AD8}/Vpr^+ infected MDMs (Unpublished results) is similar to ISGs induced by Vpr in Ad-Vpr infected MDMs. Our data indicating that Vpr leads to the induction of ISGs and activation of innate immune responses is contrary to some of the previously published reports which showed that Vpr helps HIV-1 to escape the innate immune responses by either counteracting the UNG2, a host cellular intrinsic factor which inhibits HIV-1 replication [55–57] or by manipulating the cellular SLX4 complex which is a negative regulator of Type 1 IFN production [58]. Therefore, the complex role played by Vpr in escaping HIV-1 virions from innate immune responses or by activating innate immunity through inducing ISGs in HIV-1 infected macrophages must be investigated in future studies.

Our data confirmed that HIV-1 Vpr leads to the induction of ISGs in MDMs. However, our findings showed some donor-specific differences in the expression profiles of these ISGs, which might be due to differences in overall susceptibility and the host response to the HIV-1 Vpr infection. These differences and the number of donors used in the study should not be considered a limiting factor because the expression profiles of the selected genes in all donors were independently confirmed by qRT-PCR with reproducible and consistent readouts each time (Figure 6). Furthermore, we cannot rule out the possibility that some of these ISGs are regulated by direct or indirect interactions of Vpr with cellular proteins related to the innate immune response, including cellular transcription factors such as NF-κB, AP-1, and Sp-1 [1,47].

In conclusion, our studies have identified IRF7, STAT1, ISG15, ISG20, and TRAIL as key up-regulated molecules in MDMs harboring HIV-1 Vpr. Based on previous published reports and our present data; we suggest a potential role for these genes in host defense against HIV-1 replication and infection. Future studies to elucidate the mechanisms through which Vpr up-regulates these molecules as well as their roles in HIV-1 pathogenesis will certainly improve our understanding of the replication and pathogenesis of the HIV-1.

Materials and Methods

Cell culture and preparation of human MDMs

Human cervical HeLa cells and human embryonic kidney HEK-293 cells were maintained in Dulbecco's modified Eagle's medium (DMEM; Life Technologies) supplemented with 10% heat-inactivated fetal bovine serum (FBS; Sigma) and 100 units/mL penicillin/streptomycin (Sigma). Plasmid transfection was performed using Lipofectamine 2000 (Life Technologies).

Human PBMCs were obtained using a standard Ficoll-Paque (Pharmacia) gradient from heparinized blood from healthy individuals. $CD14^+$ cells were isolated by positive selection with anti-human $CD14^+$ magnetic beads (MACS system; Miltenyi Biotec). Purity was greater than 95% (data not shown). Primary MDMs were generated by culturing $CD14^+$ cells in RPMI 1640 medium (Sigma) supplemented with 10% FBS (Cell Culture Bioscience), 5% human AB serum(Sigma), antibiotics, and GlutaMax (Gibco), and containing recombinant human macrophage colony-stimulating factor (M-CSF; PeproTech). After 7 days, cellular differentiation status was confirmed by detection of MDM surface such as CD14 and CD68 (data not shown). All participants provided written informed consent. Ethics approval for this study was granted by the RIKEN Ethics Committees [Certificate No. Wako 21–2 (3)].

Antibodies

STAT1 (#9172), phospho-STAT1 (Tyr701; #9171), and IRF-7 (#4920) rabbit polyclonal antibodies were from Cell Signaling Technology. The ISG15 mouse monoclonal antibody (MAb) (#AIS0701) was from ATGen. The TRAIL rabbit polyclonal antibody (#54008) was from ANASPEC. The ISG20 rabbit polyclonal antibody (#ARP40392-T100) was from Aviva System

Biology. The HIV-1 Vpr mouse MAb #3 was produced by immunization of synthetic peptides N'-CQAPEDQGPQREPYN-C' corresponding to amino acids 3–16 of Vpr. The APOBEC3A goat polyclonal antibody (#NB100-93428) was from Novus Biologicals. ZsGreen1 rabbit polyclonal antibody (#632474) was from Clontech Laboratories. Fluorescein isothiocyanate (FITC)-conjugated MAbs directed against the human surface markers CD14 and CD68 were from Miltenyi Biotec and used at the supplier's recommended concentrations. The β-actin (#1978) MAb and *horseradish peroxidase* (HRP)-labeled donkey anti-goat or goat anti-mouse secondary antibodies were from Sigma.

Generation of recombinant adenoviruses

Adenoviruses were constructed using the Adeno-X^{TM} expression system (Clontech Laboratories). Briefly, wild-type (wt) Vpr from HIV-1_{NL43} [59] (GenBank accession no. M 19921) was PCR-amplified with the FLAG tag incorporated using the primers GAAGCTAGCGACTACAAGGATGACGATGACAAAATGG-AACAAGCCCCAGAAGA (forward) and GCTCTAGACTAG-GATCTACTGGCTCCAT (reverse), and cloned into the pShuttle2 vector at the *Nhe*I and *Xba*I restriction sites. Similarly, the ZsGreen1 gene was PCR-amplified with the FLAG tag incorporated using the primers TAATCTAGAGACTACAAGGAT-GACGATGACAAAGCCCCTCTCCCTCCCCCCCCCCTAA (forward) and TAGCGGCCGCTCAGGGCAAGGCGGAGCC-GGAG (reverse) using the pRetroX-IRES2-ZsGreen1 plasmid (Clontech Laboratories) as a template, and then cloned into the pShuttle vector just downstream of Vpr at the *XbaI* and *Not*I restriction sites. The integrity of the generated recombinant plasmids was confirmed by DNA sequencing. Then the entire cassette (flanked by unique I-*Ceu*I and PI-*Sce*I restriction sites) was excised and ligated into Adeno-X viral DNA using the Adeno-X expression system 1, according to the manufacturer' s instructions (Clontech Laboratories).

Adeno-X viral DNA containing the FLAG-Vpr or ZsGreen1 was linearized with *Pac*I and transfected into HEK293 cells with Lipofectamine 2000 (Life Technologies). The recombinant adenoviruses were purified using the Adeno-X maxi purification kit (Clontech Laboratories) and titrated using the Adeno-X rapid titer kit (Clontech Laboratories), following the recommendations of the manufacturer. The virus stocks were stored at −80°C for future use.

RNA extraction

MDMs were transduced with Ad-Vpr or Ad-Zs at a MOI of 100. The cells were harvested for RNA extraction at 48 h post-transduction. MDMs were washed three times with ice-cold PBS, and total RNA was extracted using the RNeasy mini kit with DNase digestion, according to the manufacturer's instructions (QIAGEN). RNA was quantified using a NanoDrop spectrophotometer (Thermo Fisher) and stored at −80°C. For microarray analysis, the quality of the RNA was determined using the Agilent Bioanalyzer (Agilent Technologies).

Microarray and data analysis

RNA samples were analyzed by microarray using the GeneChip Human Genome U133 2.0 plus array (Affymetrix). Microarray hybridization and fluorescence detection were performed as described in the Affymetrix GeneChip Expression Analysis Technical Manual. The. cel data files generated by the Affymetrix microarray hybridization platform were analyzed using GeneSpring GX ver. 12.0 software (Agilent Technologies). Probe-level analysis was performed using the RMA algorithm. Microarray data have been deposited in NCBI's Gene Expression Omnibus and assigned the GEO Series accession number GSE56591. Fold changes in gene expression, hierarchical clustering, and gene ontology annotations were determined.

Real-time qRT-PCR analysis of differentially expressed genes

Total RNA was prepared using the RNeasy mini kit as described above. RT-PCR was performed using specific primers and One-Step SYBR Green PCR mix (Takara), according to the manufacturer's manual. qRT-PCR was performed using a Prism 7500 sequence detection system (Applied Biosystems). Samples were run in triplicate and all data were normalized to *GAPDH* mRNA expression as an internal control.

Western blotting

Mock or virus-infected MDMs were washed with PBS and then lysed with CelLytic^{TM} MT Cell Lysis reagent (Sigma) which was supplemented with a protease inhibitor cocktail (Roche Diagnostics) according to the manufacturer's instructions. Protein concentrations were determined with a BCA protein assay kit (Pierce) using bovine serum albumin as a standard. Proteins were separated by sodium dodecyl sulfate-10% polyacrylamide gel electrophoresis (SDS-PAGE) and transferred to polyvinyl difluoride (PVDF; Millipore Corp.) membranes. The PVDF membranes were probed with the primary antibodies mentioned above followed by an anti-mouse HRP or anti-goat HRP or anti-rabbit HRP secondary antibody (Sigma), and signals were detected by enhanced chemiluminescence (GE Healthcare).

Analysis of the cell cycle

HeLa cells were infected with an adenoviral vector expressing Vpr or expressing only ZsGreen1, as a control. At 48 h post-infection, the cells were harvested and fixed with 1% formaldehyde followed by 70% ethanol. Fixed cells were incubated in PBS containing RNase A (50 μg/ml) at 37°C for 20 min and then stained with PI (40 μg/ml). For each sample, at least 7,000 cells were analyzed using a FACS Calibur instrument (Becton-Dickinson) with CELL Quest software (Becton-Dickinson). Ratios of the numbers of cells in the G1 and G2/M phases (G2+M: G1 ratios) were calculated using ModFit LT Software (Verity Software House).

Acknowledgments

The authors thank Mr. Keisuke Fukumoto for his technical assistance. We are grateful *to* the RIKEN Support Unit for Bio-material Analysis, and the RIKEN BSI Research Resources Center for assistance with the microarray and sequence analyses.

Author Contributions

Conceived and designed the experiments: YA MAZ. Performed the experiments: MAZ TM HS GX. Analyzed the data: YA MAZ GX TM HS. Contributed reagents/materials/analysis tools: YA. Contributed to the writing of the manuscript: YA MAZ. The submission of microarray data to the NCBI's Gene Expression Omnibus: ST MAZ.

References

1. Herbein G, Gras G, Khan KA, Abbas W (2010) Macrophage signaling in HIV-1 infection. Retrovirology 7: 34.
2. Kilareski EM, Shah S, Nonnemacher MR, Wigdahl B (2009) Regulation of HIV-1 transcription in cells of the monocyte-macrophage lineage. Retrovirology 6: 118.
3. Barrero CA, Datta PK, Sen S, Deshmane S, Amini S, et al. (2013) HIV-1 Vpr modulates macrophage metabolic pathways: a SILAC-based quantitative analysis. PLoS One 8: e68376.
4. Carlson KA, Ciborowski P, Schellpeper CN, Biskup TM, Shen RF, et al. (2004) Proteomic fingerprinting of HIV-1-infected human monocyte-derived macrophages: a preliminary report. J Neuroimmunol 147: 35–42.
5. Van den Bergh R, Florence E, Vlieghe E, Boonefaes T, Grooten J, et al. (2010) Transcriptome analysis of monocyte-HIV interactions. Retrovirology 7: 53.
6. Tristem M, Marshall C, Karpas A, Hill F (1992) Evolution of the primate lentiviruses: evidence from vpx and vpr. Embo J 11, 3405–3412.
7. Murakami T, Aida Y (2014) Visualizing Vpr-induced G2 arrest and apoptosis. PLoS One 9: e86840.
8. Nonaka M, Hashimoto Y, Takeshima SN, Aida Y (2009) The human immunodeficiency virus type 1 Vpr protein and its carboxy-terminally truncated form induce apoptosis in tumor cells. Cancer Cell Int 9: 20.
9. Nishizawa M, Kamata M, Katsumata R, Aida Y (2000) A carboxy-terminally truncated form of the human immunodeficiency virus type 1 Vpr protein induces apoptosis via G(1) cell cycle arrest. J Virol 74: 6058–6067.
10. Aida Y, Matsuda G (2009) Role of Vpr in HIV-1 nuclear import: therapeutic implications. Curr HIV Res 7: 136–143.
11. Nitahara-Kasahara Y, Kamata M, Yamamoto T, Zhang X, Miyamoto Y, et al. (2007) Novel nuclear import of Vpr promoted by importin alpha is crucial for human immunodeficiency virus type 1 replication in macrophages. J Virol 81: 5284–5293.
12. Takeda E, Murakami T, Matsuda G, Murakami H, Zako T, et al. (2011) Nuclear exportin receptor CAS regulates the NPI-1-mediated nuclear import of HIV-1 Vpr. PLoS One 6: e27815.
13. Popov S, Rexach M, Zybarth G, Reiling N, Lee MA, et al. (1998) Viral protein R regulates nuclear import of the HIV-1 pre-integration complex. Embo J 17: 909–917.
14. Kamata M, Nitahara-Kasahara Y, Miyamoto Y, Yoneda Y, Aida Y (2005) Importin-alpha promotes passage through the nuclear pore complex of human immunodeficiency virus type 1 Vpr. J Virol 79: 3557–3564.
15. Felzien LK, Woffendin C, Hottiger MO, Subbramanian RA, Cohen EA, et al. (1998) HIV transcriptional activation by the accessory protein, VPR, is mediated by the p300 co-activator. Proc Natl Acad Sci U S A 95: 5281–5286.
16. Hashizume C, Kuramitsu M, Zhang X, Kurosawa T, Kamata M, et al. (2007) Human immunodeficiency virus type 1 Vpr interacts with spliceosomal protein SAP145 to mediate cellular pre-mRNA splicing inhibition. Microbes Infect 9: 490–497.
17. Kuramitsu M, Hashizume C, Yamamoto N, Azuma A, Kamata M, et al. (2005) A novel role for Vpr of human immunodeficiency virus type 1 as a regulator of the splicing of cellular pre-mRNA. Microbes Infect 7: 1150–1160.
18. Ayyavoo V, Mahalingam S, Rafaeli Y, Kudchodkar S, Chang D, et al. (1997) HIV-1 viral protein R (Vpr) regulates viral replication and cellular proliferation in T cells and monocytoid cells in vitro. J Leukoc Biol 62: 93–99.
19. Hrecka K, Gierszewska M, Srivastava S, Kozaczkiewicz L, Swanson SK, et al. (2007) Lentiviral Vpr usurps Cul4-DDB1[VprBP] E3 ubiquitin ligase to modulate cell cycle. Proc Natl Acad Sci U S A 104: 11778–11783.
20. Planelles V, Benichou S (2009) Vpr and its interactions with cellular proteins. Curr Top Microbiol Immunol 339: 177–200.
21. Sherman MP, De Noronha CM, Williams SA, Greene WC (2002) Insights into the biology of HIV-1 viral protein R. DNA Cell Biol 21: 679–688.
22. Balotta C, Lusso P, Crowley R, Gallo RC, Franchini G (1993) Antisense phosphorothioate oligodeoxynucleotides targeted to the vpr gene inhibit human immunodeficiency virus type 1 replication in primary human macrophages. J Virol 67: 4409–4414.
23. Connor RI, Chen BK, Choe S, Landau NR (1995) Vpr is required for efficient replication of human immunodeficiency virus type-1 in mononuclear phagocytes. Virology 206: 935–944.
24. Dedera D, Hu W, Vander Heyden N, Ratner L (1989) Viral protein R of human immunodeficiency virus types 1 and 2 is dispensable for replication and cytopathogenicity in lymphoid cells. J Virol 63: 3205–3208.
25. Lavallee C, Yao XJ, Ladha A, Gottlinger H, Haseltine WA, et al. (1994) Requirement of the Pr55gag precursor for incorporation of the Vpr product into human immunodeficiency virus type 1 viral particles. J Virol 68: 1926–1934.
26. Zhou T, Dang Y, Baker JJ, Zhou J, Zheng YH (2012) Evidence for Vpr-dependent HIV-1 replication in human CD4+ CEM.NKR T-cells. Retrovirology 9: 93.
27. Schoggins JW, Rice CM (2011) Interferon-stimulated genes and their antiviral effector functions. Curr Opin Virol 1: 519–525.
28. Sadler AJ, Williams BR (2008) Interferon-inducible antiviral effectors. Nat Rev Immunol 8: 559–568.
29. Huang Y, Walstrom A, Zhang L, Zhao Y, Cui M, et al. (2009) Type I interferons and interferon regulatory factors regulate TNF-related apoptosis-inducing ligand (TRAIL) in HIV-1-infected macrophages. PLoS One 4: e5397.
30. Kohler JJ, Tuttle DL, Coberley CR, Sleasman JW, Goodenow MM (2003) Human immunodeficiency virus type 1 (HIV-1) induces activation of multiple STATs in CD4+ cells of lymphocyte or monocyte/macrophage lineages. J Leukoc Biol 73: 407–416.
31. Nasr N, Maddocks S, Turville SG, Harman AN, Woolger N, et al. (2012) HIV-1 infection of human macrophages directly induces viperin which inhibits viral production. Blood 120: 778–788.
32. Okumura A, Lu G, Pitha-Rowe I, Pitha PM (2006) Innate antiviral response targets HIV-1 release by the induction of ubiquitin-like protein ISG15. Proc Natl Acad Sci U S A 103: 1440–1445.
33. Pincetic A, Kuang Z, Seo EJ, Leis J (2010) The interferon-induced gene ISG15 blocks retrovirus release from cells late in the budding process. J Virol 84: 4725–4736.
34. Sirois M, Robitaille L, Allary R, Shah M, Woelk CH, et al. (2011) TRAF6 and IRF7 control HIV replication in macrophages. PLoS One 6: e28125.
35. Wang X, Chao W, Saini M, Potash MJ (2011) A common path to innate immunity to HIV-1 induced by Toll-like receptor ligands in primary human macrophages. PLoS One 6: e24193.
36. Janket ML, Manickam P, Majumder B, Thotala D, Wagner M, et al. (2004) Differential regulation of host cellular genes by HIV-1 viral protein R (Vpr): cDNA microarray analysis using isogenic virus. BiochemBiophys Res Commun 314(4): 1126–32.
37. Vázquez N, Greenwell-Wild T, Marinos NJ, Swaim WD, Nares S, et al. (2005) Human immunodeficiency virus type 1-induced macrophage gene expression includes the p21 gene, a target for viral regulation. J Virol79(7): 4479–91.
38. Darnell JE Jr (1997) STATs and gene regulation. Science 277: 1630–1635.
39. Kane M, Yadav SS, Bitzegeio J, Kutluay SB, Zang T, et al. (2013) MX2 is an interferon-induced inhibitor of HIV-1 infection. Nature 502: 563–566.
40. Honda K, Yanai H, Negishi H, Asagiri M, Sato M, et al. (2005) IRF-7 is the master regulator of type-I interferon-dependent immune responses. Nature 434: 772–777.
41. Marie I, Durbin JE, Levy DE (1998) Differential viral induction of distinct interferon-alpha genes by positive feedback through interferon regulatory factor-7. Embo J 17: 6660–6669.
42. Shuai K, Liu B (2003) Regulation of JAK-STAT signalling in the immune system. Nat Rev Immunol 3: 900–911.
43. Takeda K, Akira S (2000) STAT family of transcription factors in cytokine-mediated biological responses. Cytokine Growth Factor Rev 11: 199–207.
44. Pilz A, Ramsauer K, Heidari H, Leitges M, Kovarik P, et al. (2003) Phosphorylation of the Stat1 transactivating domain is required for the response to type I interferons. EMBO Rep 4: 368–373.
45. Bovolenta C, Camorali L, Lorini AL, Ghezzi S, Vicenzi E, et al. (1999) Constitutive activation of STATs upon in vivo human immunodeficiency virus infection. Blood 94: 4202–4209.
46. Chaudhuri A, Yang B, Gendelman HE, Persidsky Y, Kanmogne GD (2008) STAT1 signaling modulates HIV-1-induced inflammatory responses and leukocyte transmigration across the blood-brain barrier. Blood 111: 2062–2072.
47. Ayyavoo V, Mahboubi A, Mahalingam S, Ramalingam R, Kudchodkar S, et al. (1997) HIV-1 Vpr suppresses immune activation and apoptosis through regulation of nuclear factor kappa B. Nat Med 3: 1117–1123.
48. Espert L, Degols G, Lin YL, Vincent T, Benkirane M, et al. (2005) Interferon-induced exonuclease ISG20 exhibits an antiviral activity against human immunodeficiency virus type 1. J Gen Virol 86: 2221–2229.
49. Herbeuval JP, Boasso A, Grivel JC, Hardy AW, Anderson SA, et al. (2005) TNF-related apoptosis-inducing ligand (TRAIL) in HIV-1-infected patients and its in vitro production by antigen-presenting cells. Blood 105: 2458–2464.
50. Lum JJ, Pilon AA, Sanchez-Dardon J, Phenix BN, Kim JE, et al. (2001) Induction of cell death in human immunodeficiency virus-infected macrophages and resting memory CD4 T cells by TRAIL/Apo2l. J Virol 75: 11128–11136.
51. Huang Y, Erdmann N, Peng H, Herek S, Davis JS, et al. (2006) TRAIL-mediated apoptosis in HIV-1-infected macrophages is dependent on the inhibition of Akt-1 phosphorylation. J Immunol 177: 2304–2313.
52. Laforge M, Campillo-Gimenez L, Monceaux V, Cumont MC, Hurtrel B, et al. (2011) HIV/SIV infection primes monocytes and dendritic cells for apoptosis. PLoS Pathog 7: e1002087.
53. Foley JF, Yu CR, Solow R, Yacobucci M, Peden KW, et al. (2005) Roles for CXC chemokine ligands 10 and 11 in recruiting CD4+ T cells to HIV-1-infected monocyte-derived macrophages, dendritic cells, and lymph nodes. J Immunol 174: 4892–4900.
54. Poon B, Grovit-Ferbas K, Stewart SA, Chen IS (1998) Cell cycle arrest by Vpr in HIV-1 virions and insensitivity to antiretroviral agents. Science281(5374): 266–9.
55. Fenard D, Houzet L, Bernard E, Tupin A, Brun S, et al. (2009) Uracil DNA Glycosylase 2 negatively regulates HIV-1 LTR transcription. Nucleic Acids Res37(18): 6008–1.
56. Langevin C, Maidou-Peindara P, Aas PA, Jacquot G, Otterlei M, et al. (2009) Human immunodeficiency virus type 1 Vpr modulates cellular expression of UNG2 via a negative transcriptional effect. J Virol 83(19): 10256–63.
57. Nekorchuk MD, Sharifi HJ, Furuya AK, Jellinger R, de Noronha CM (2013) HIV relies on neddylation for ubiquitin ligase-mediated functions. Retrovirology10: 138.

58. Laguette N, Brégnard C, Hue P, Basbous J, Yatim A, et al. (2014) Premature activation of the SLX4 complex by Vpr promotes G2/M arrest and escape from innate immune sensing. Cell156(1–2): 134–45.

59. Adachi A, Gendelman HE, Koenig S, Folks T, Willey R, et al. (1986) Production of acquired immunodeficiency syndrome-associated retrovirus in human and nonhuman cells transfected with an infectious molecular clone. J Virol 59: 284–291.

PLOS | ONE

RESEARCH ARTICLE

Crystal Structure of Human Importin-α1 (Rch1), Revealing a Potential Autoinhibition Mode Involving Homodimerization

Hideyuki Miyatake[1]*, Akira Sanjoh[2], Satoru Unzai[3], Go Matsuda[4], Yuko Tatsumi[2], Yoichi Miyamoto[5,6], Naoshi Dohmae[1], Yoko Aida[4]*

1 Global Research Cluster Collaboration Promotion Unit, RIKEN, 2–1, Hirosawa, Wako-shi, Saitama 351–0198, Japan, **2** Protein Wave Corporation, 1–16–5 Nishitomigaoka, Nara 631–0006, Japan, **3** Graduate School of Medical Life Science, Yokohama City University, 1–7–29 Suehiro-cho, Tsurumi-ku, Yokohama 230–0045, Japan, **4** Viral Infectious Diseases Unit, RIKEN, 2–1, Hirosawa, Wako-shi 351–0198, Japan, **5** Department of Biochemistry and Molecular Biology, School of Biomedical Sciences, Monash University, Building 76 Level 2, Wellington Road, Clayton VIC 3800, Australia, **6** Laboratory of Nuclear Transport Dynamics, National Institute of Biomedical Innovation, 7–6–8 Saito-Asagi, Ibaraki-shi, Osaka 567–0085, Japan

* miyatake@riken.jp (HM); aida@riken.jp (YA)

OPEN ACCESS

Citation: Miyatake H, Sanjoh A, Unzai S, Matsuda G, Tatsumi Y, Miyamoto Y, et al. (2015) Crystal Structure of Human Importin-α1 (Rch1), Revealing a Potential Autoinhibition Mode Involving Homodimerization. PLoS ONE 10(2): e0115995. doi:10.1371/journal.pone.0115995

Academic Editor: Ivano Eberini, Università degli Studi di Milano, ITALY

Received: February 15, 2014

Accepted: December 3, 2014

Published: February 6, 2015

Funding: This work was partly supported by the RIKEN incentive research grant (to HM), and also by a Health Sciences Research Grant from the Ministry of Health, Labor and Welfare of Japan (Research on HIV/AIDS) and by the program for Promotion of Fundamental Studies in Health Sciences of the National Institute of Biomedical Innovation (NIBIO) of Japan (to YA).

Competing Interests: The authors have read the journal's policy and have the following conflicts: Akira Sanjoh is a president of the Protein Wave Corporation and Yuko Tatsumi is employed by the

Abstract

In this study, we determined the crystal structure of N-terminal importin-β-binding domain (IBB)-truncated human importin-α1 (ΔIBB-h-importin-α1) at 2.63 Å resolution. The crystal structure of ΔIBB-h-importin-α1 reveals a novel closed homodimer. The homodimer exists in an autoinhibited state in which both the major and minor nuclear localization signal (NLS) binding sites are completely buried in the homodimerization interface, an arrangement that restricts NLS binding. Analytical ultracentrifugation studies revealed that ΔIBB-h-importin-α1 is in equilibrium between monomers and dimers and that NLS peptides shifted the equilibrium toward the monomer side. This finding suggests that the NLS binding sites are also involved in the dimer interface in solution. These results show that when the IBB domain dissociates from the internal NLS binding sites, e.g., by binding to importin-β, homodimerization possibly occurs as an autoinhibition state.

Introduction

In eukaryotic cells, the cytoplasm and the nucleus are divided by the nuclear membrane. The nuclear pore complex (NPC), situated on the nuclear membrane, acts as a gate that allows free diffusion of particles, such as small molecules and ions of less than ~9 nm [1–3]. Particles that are larger than 40 kDa and comprise proteins or protein–nucleic acid complexes are transported through the NPC by a variety of active transport mechanisms [4], [5]. Systems consisting of importin α/β have been intensively studied [6–8]. Human importin-αs (h-importin-αs) comprise at least seven isoforms: h-importin-α1 (Rch1/KPNA2), h-importin-α3 (Qip1/KPNA4), h-importin-α4 (KPNA3), h-importin-α5 (NPI-1/KPNA1), h-importin-α6 (KPNA5), h-importin-α7 (KPNA6), and h-importin-α8 (KPNA7) [9], [10]. In addition, at least 23 kinds

of human importin-βs have been identified. In a typical scenario of importin-α/β transportation, the flexible N-terminus importin-β binding domain (IBB) binds to the NLS binding sites of importin-α in an autoinhibition manner. When the importin-α complexes to the importin-β with the IBB domain, it dissociates from the NLS binding sites. Then the cargo proteins tagged with the basic nuclear localization signal (NLS) sequence can bind to the exposed NLS binding sites on the surface of importin-α. Finally, hetero-trimer, importin-αfiβ and the cargo protein is formed.

Importin-α works as an adaptor molecule to connect importin-β and the NLS cargo, which makes it possible for the limited variety of importin-βs to bind to a large variety of NLS cargoes. The hetero-trimer is then transported into the nucleus through the NPC, with the importin-β working as an active engine. Such a transportation system ensures that larger cargoes (Mw > 40 kDa) can travel through the NPC into the nucleus [9–12]. There seems to be some mechanism in the isoforms of human importin-αs that is responsible for the diversity of binding to a variety of NLS cargoes, even though the whole structures of the subfamilies closely resemble each other. On the other hand, some importin-αs are known to form homodimers. The crystal structure of yeast importin-α was first reported as a homodimer [13]. In the homodimer, major and minor NLS binding sites are still exposed to solution; thus, NLS peptides can bind to the sites. In addition, *Xenopus* importin-α seems to form homodimers or multimers during purification [14]. However, the functional aspects of these multimerization properties of importin-αs have not been resolved.

Here, we report homodimeric human importin-α1 (h-importin-α1) by the use of X-ray crystallography and shed light on the solution state of the homodimerization in relation to NLS binding by using analytical ultracentrifugation (AUC) and isothermal titration calorimetry (ITC).

Materials and Methods

Expression system construction

Full-length human importin-α1 (h-importin-α1) (1–526) was generated from pGEX6P3/importin-α1-Flag, as previously described [15], by site-directed mutagenesis, resulting in a Phe-to-Stop substitution at amino acid 527. IBB domain-truncated h-importin-α1 (Δ-h-importin-α1) (1–10, 55–529) was generated from pGEX6P3/importin-α1-His_6, as previously described, by inverse polymerase chain reaction (PCR) amplification using the following primers: forward, 5′-*TCA TTT CCT GAT GAT GCT ACT TCT CCG CTG*-3′, and reverse, 5′-*TGG TGT ATT AGC ATT CTC GTT GGT GGA CAT*-3′. The PCR product was digested with *Bam*HI and *Not*I and cloned into pGEX6P3. All constructs were verified by DNA sequencing.

Protein preparation

h-importin-α1 (1–526) and ΔIBB-h-importin-α1 were overexpressed by *E. coli* strain BL21 (DE3) Codonplus-RIL (Stratagene) and purified as follows: Frozen cells (10 g) obtained from a 1 L culture were suspended in 100 mL of sonication buffer (50 mM tris(hydroxymethyl)aminomethane (Tris)-HCl, 500 mM NaCl, 1 mM dithiothreitol (DTT), 1 mM ethylenediaminetetraacetic acid (EDTA), pH 8.0) and lysed by sonication using an Ultrasonic Processor VCX 500 (Sonics & Materials, Inc.). The lysate was collected and centrifuged at 15,000 rpm for 1 h. The supernatant was filtered through a 0.45 μm HT Tuffryn membrane syringe filter (Pall Corporation). A GSTrap FF column (GE Healthcare) packed with Glutathione Sepharose 4 Fast Flow (GE Healthcare) was pre-equilibrated with phosphate-buffered saline (PBS) buffer. This lysate was then loaded onto a column at a flow rate of 1 mL/min. After washing with 50 mL wash buffer (50 mM Tris-HCl, 150 mM NaCl, 1 mM DTT, 10% glycerol, 1 mM EDTA, pH 8.0),

bound GST-tagged h-importin-α1 was eluted with 30 mL elution buffer (50 mM Tris-HCl, 150 mM NaCl, 1 mM DTT, 10% glycerol, 1 mM EDTA, 5 mM reduced glutathione, pH 8.2). Elution fractions containing GST-h-importin-α1 and GST-ΔIBB-h-importin-α1 were pooled. The PreScission protease (GE Healthcare) was incubated with the pooled fractions according to the manufacturer's instructions, and the solution was dialyzed against 2 L of digestion buffer (50 mM Tris-HCl, 150 mM NaCl, 1 mM DTT, 1 mM EDTA, 0.01% Triton X-100, pH 7.5) for 12 h at 277 K. The digested protein was filtered through a 0.45 μm HT Tuffryn membrane syringe filter and loaded onto a GSTrap FF column (GE Healthcare). The cleaved h-importin-α1 and ΔIBB-h-importin-α1 were collected in the flow-through and washed fractions. The protein samples were diluted to obtain an NaCl concentration of 75 mM and a pH of 8.0 with 20 mM Tris-HCl, 1 mM DTT, 1 mM EDTA, and 10% glycerol. The samples were loaded onto a Resource-Q column (GE Healthcare) packed with SOURCE 15Q (GE Healthcare) (S1 Fig.). For elution, the column was developed with a linear gradient from 0 to 500 mM NaCl in 20 mM Tris-HCl, 1 mM DTT, 1 mM EDTA, 10% glycerol, pH 8.0, at a flow rate of 0.2 mL/min. The eluted fractions of interest were pooled and concentrated with a Centriprep YM-10 centrifugal device (Amicon/Millipore) to a concentration of 10 mg/mL and used for the ITC and AUC-SV experiments. For the crystallization experiments, these fractions were filtered and loaded in a pre-equilibrated HiLoad 16/60 Superdex 75 size exclusion column (GE Healthcare) with 20 mM Tris-HCl, pH 8.0, 200 mM NaCl, and 5 mM DTT. The eluted fractions were collected and concentrated with the Centriprep YM-10 to 10 mg/mL.

Peptide synthesis

SV40 NLS (PKKKRKV) and nucleoplasmin NLS (KRPAATKKAGQAKKKK) peptides were synthesized by stepwise solid-phase synthesis on a 433A peptide synthesizer (Applied Biosystems) using a standard 9-fluorenylmethyloxycarbonyl strategy (amino acid activated and coupled with 2-(1H-benzotriazol-1-yl)-1,1,3,3-tetramethyluronium hexafluorophosphate/ 1-hydroxybenzotriazole/N,N-diisopropylethylamine) on a 0.1 mM scale.

Analytical ultracentrifugation (AUC)

AUC sedimentation velocity (AUC-SV) experiments were carried out in AUC buffer (0.1 M Tris-HCl, pH 8.0, 0.2 M NaCl, 1 mM tris(2-carboxyethyl)phosphine (TCEP)), using an Optima XL-I analytical ultracentrifuge equipped with two optical systems, the Rayleigh interference and absorbance systems (Beckman Coulter). For AUC-SV measurements, 10 mg/mL h-importin-α1 and ΔIBB-h-importin-α1 samples were diluted with the AUC buffer. Then, 4 mM SV40 and nucleoplasmin NLS solutions, dissolved in the AUC buffer, were added to the sample solution. The AUC-SV measurements were conducted at 50,000 rpm at a temperature of 293 K, using an An-50 Ti rotor featuring cells with a standard 12-mm charcoal-epon double sector centerpiece and sapphire windows. During the runs, changes in the concentration gradient were monitored with a Rayleigh interference optical system or absorbance at 280 nm. All of the AUC-SV raw data were analyzed by the program SEDFIT14.1, with the continuous $C(s)$ distribution model [16]. The SEPHAT 10.58d program was used for analysis of the isotherm of weight-average s-values. A monomer-dimer self-association model was applied [17].

Isothermal titration calorimetry (ITC)

We investigated the binding of SV40 NLS and nucleoplasmin NLS to h-importin-α1 and ΔIBB-h-importin-α1. ITC measurements were carried out using a MicroCal iTC_{200} (GE Healthcare) in 0.1 M Tris-HCl, pH 8.0, 0.2 M NaCl, and 5 μM DTT at 293 K. The cell chamber was loaded with 200 μL of 15 μM h-importin-α1 and titrated 20 times with 2 mM of SV40 NLS

solution or 2 mM nucleoplasmin NLS solution, while stirring at 1,000 rpm. The data analysis was performed with Origin software equipped with the ITC (Fig. 3A). ΔIBB-h-importin-α1 (17 μM) was used for the ITC experiment with 40 titrations for SV40 NLS binding and 30 titrations for nucleoplasmin NLS (Fig. 3B, C).

Crystallization of ΔIBB-h-importin-α1

The crystals of ΔIBB-importin-α1 were prepared at 293 K using the sitting drop vapor diffusion method with 5.0 μL of the concentrated protein solutions (10 mg/mL) and an equal volume of precipitant buffer (50 mM 2-(N-morpholino)ethanesulfonic acid (MES) pH 5.5, 100 mM ammonium sulfate, 10 mM $MgCl_2$, 15–20% (w/v) polyethylene glycol (PEG) 8000). Crystals appeared within 2 days and grew to a size of 0.5 mm in 2 weeks.

Diffraction data collection, structure determination and validation

All diffraction data were collected at the BL26B2 station of SPring-8 using the mail-in data collection system [18], [19]. The crystals were soaked in the solution containing 30% (w/v) PEG 8000 as a cryoprotectant and flash-frozen at 100 K. The diffraction data were processed using the HKL2000 package [20]. The molecular replacement technique was executed using the MrBump package [21] using the truncated molecular model (84–476) of importin-α5 (PDB ID: 2JDQ) as a template, which gave two solutions in the asymmetric unit. The initial model was improved using RESOLVE [22] and further refined using LAFIRE [23] and ARP/wARP packages [24]. The model was manually rebuilt with the help of XtalView [25] and Coot [26], and refined with CNS [27] and PHENIX [28]. The current model of the ΔIBB-importin-α1 involves the residues of 75–496 (chain A) and 75–497 (chain B) with an R/R_{free} factor of 0.193/0.221. The structural validation was performed with the Procheck [29] and MolProbity [30] programs. The coordinate and structure factors of ΔIBB-h-importin-α1 have been deposited at the Protein Data Bank with PDB ID: 3WPT.

Results

Expression and purification of h-importin-α1 and ΔIBB-h-importin-α1

h-importin-α1 and ΔIBB-h-importin-α1 were expressed by the *E. coli* strain BL21 (DE3) Codonplus-RIL (Stratagene). S1 Fig. shows the chromatograms corresponding to elution from an anion exchange column (Resource Q) used for the purification of h-importin-α1 and ΔIBB-h-importin-α1.

AUC-SV experiments

ΔIBB-h-importin-α1. The AUC-SV for ΔIBB-h-importin-α1 shows that it is in a concentration-dependent monomer–dimer equilibrium (Fig. 1A, B). The *C*(*s*) distributions are characterized by two peaks, one at 3.1–3.3 S and one at 3.9 S; the relative sizes of the peaks vary with protein concentration, and they are interpreted as corresponding to monomer and dimer, respectively. The *C*(*s*) distributions were used to create a weight average S value (sw) isotherm. We calculated the sw by integration of the *C*(*s*) curves between 2.5 S and 5.0 S for each protein concentration, and then plotted the sw vs protein concentration using SEDPHAT (Fig. 1C). The monomer–dimer self-association model was applied for the curve fitting. The monomer–dimer KD is estimated to be 8 ± 3 μM. The NLS ligands, SV40 and NP, shift the equilibrium to the monomer side (Fig. 1D, E). These results show that the NLS binding sites are involved in the dimer interface in solution.

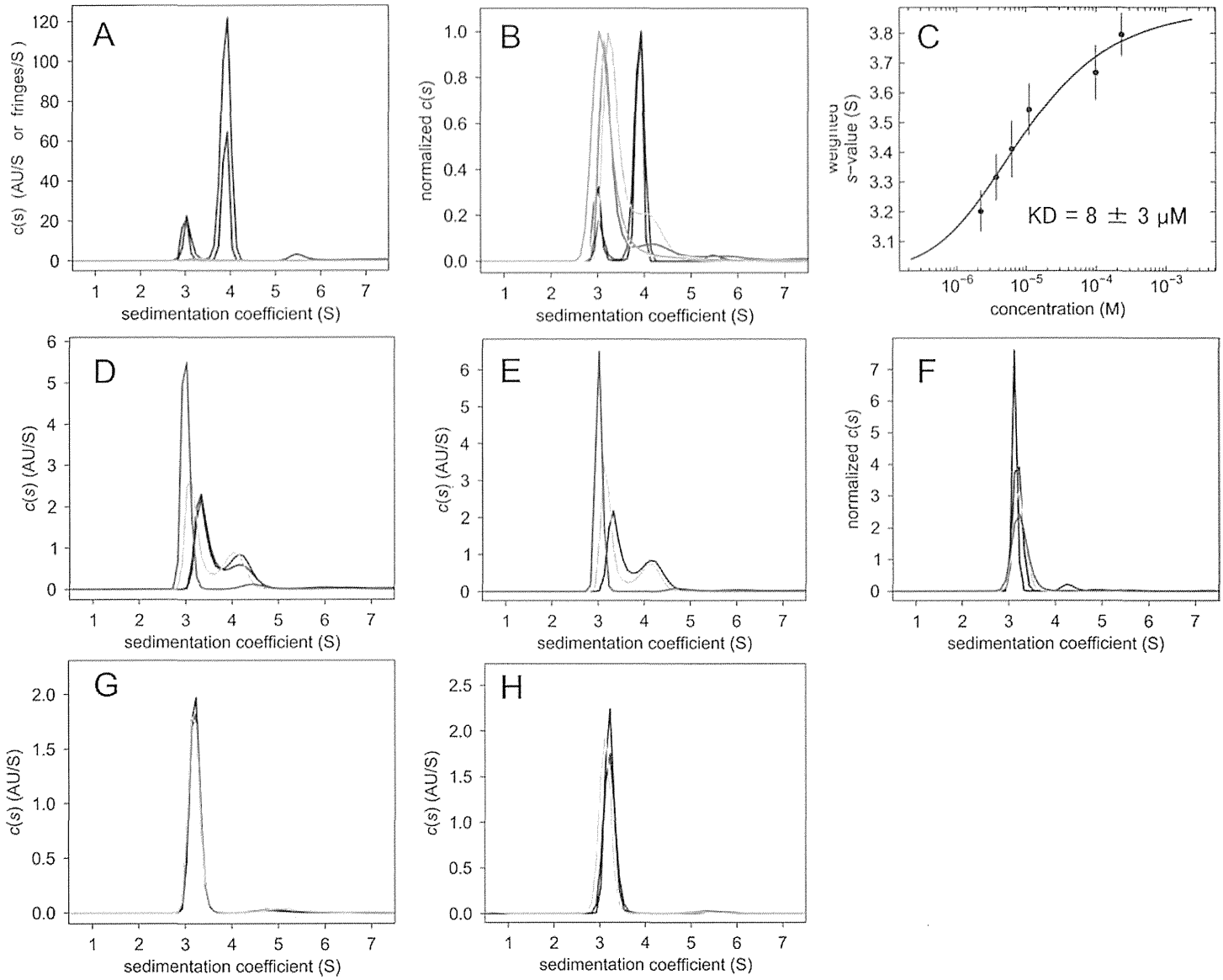

Fig 1. AUC-SV measurements. (A) c(s) distributions of ΔIBB-h-importin-α1, 247 μM (purple), 100 μM (blue), 14 μM (cyan), 11 μM (green), 7.3 μM (yellow) and 4.2 μM (orange). (B) Normalized c(s) distributions of ΔIBB-h-importin-α1. (C) KD value estimation by the fitting curve of the sw vs protein concentration. (D) 25 μM ΔIBB-h-importin-α1 + SV40 NLS of 0 μM (purple), 1 μM (blue), 10 μM (cyan) and 100 μM (green). (E) 25 μM ΔIBB-h-importin-α1 + nucleoplasmin NLS of 0 μM (purple), 10 μM (cyan), and 100 μM (green). (F) Normalized c(s) distributions of h-importin-α1, 61 μM (purple), 34 μM (blue), 8.6 μM (cyan), and 4.3 μM (green). (G) 10 μM h-importin-α1 + SV40 NLS of 0 μM (purple), 10 μM (blue), 100 μM (cyan). (H) 10 μM h-importin-α1 + nucleoplasmin NLS of 0 μM (purple), 10 μM (blue), 100 μM (cyan).

doi:10.1371/journal.pone.0115995.g001

h-importin-α1. However, h-importin-α1 remains monomeric in a variety of protein concentration (Fig. 1F). Neither of the SV40 nor NP NLS peptides changed the monomeric state (Fig. 1G, H). These results show that the self-bound IBB domain autoinhibits not only NLS binding but also homodimerization.

X-ray crystallography of ΔIBB-h-importin-α1

Only the diffractive crystals of ΔIBB-h-importin-α1 were obtained, not those of h-importin-α1. The crystals diffracted X-rays to 2.6 Å resolution in SPring-8. The molecular replacement technique was used to solve the structure (Table 1). The crystal structure of ΔIBB-importin-α1 is shown in Fig. 2A. The pseudo 2-fold axis lies in close proximity to the N239 of chains A and

Table 1. Crystallographic data collection and refinement statistics of ΔIBB-h-importin-α1.

Space group	Tetragonal $P4_32_12$
Cell constants (Å)	$a = b = 139.30$, $c = 141.29$
Wavelength (Å)	1.00
Resolution (Å)	50.0–2.60 (2.69–2.60)
Oscillation angle (deg.)	1.0
σcut-off	0.0
R_{merge} [a]	0.065 (0.391)
No. of measurements	352,972 (3,701)
No. of independent reflections	40,652
Completeness (%)	96.96 (90.25)
Multiplicity	8.7 (4.8)
Mean <I/ σ(I)>	31.83 (4.86)
Wilson B-factor (Å)	48.59
Refinement statistics	
Resolution (Å)	46.7–2.63 (2.79–2.63)
No. of reflections used	40,616 (5,982)
Completeness (%)	96.96 (90.25)
R_{work} [b]	0.1930 (0.2843)
R_{free} [c]	0.2207 (0.3062)
No. of atoms	
Protein (chain A, chain B)	6,496, 6,507
PEG	11
Water	192
Average B factor	
Protein (chin A, chain B)	45.879, 38.836
PEG	71.622
Water	39.057
R.m.s. deviations	
Bond lengths (Å)	0.003
Bond angles (°)	0.671
Ramachandran plot (%)	
Favored region	95.6
Allowed region	4.04
Outer region	0.36
Clashscore[d]	12.08

[a] $R_{merge} = \Sigma\Sigma_i \, ||I(h)—I(h)_i| \, / \, \Sigma\Sigma_i \, I(h)$, where $I(h)$ is the mean intensity after rejections.

[b] $R_{work} = \Sigma| \, F_p—F_{pc} \, /\Sigma \, |F_p|$.

[c] R_{free}, the same as R_{work} but calculated on 4.93% of data excluded from refinement.

[d] Clashscore, calculated by MolProbity.

Values in parentheses are for highest resolution shells.

doi:10.1371/journal.pone.0115995.t001

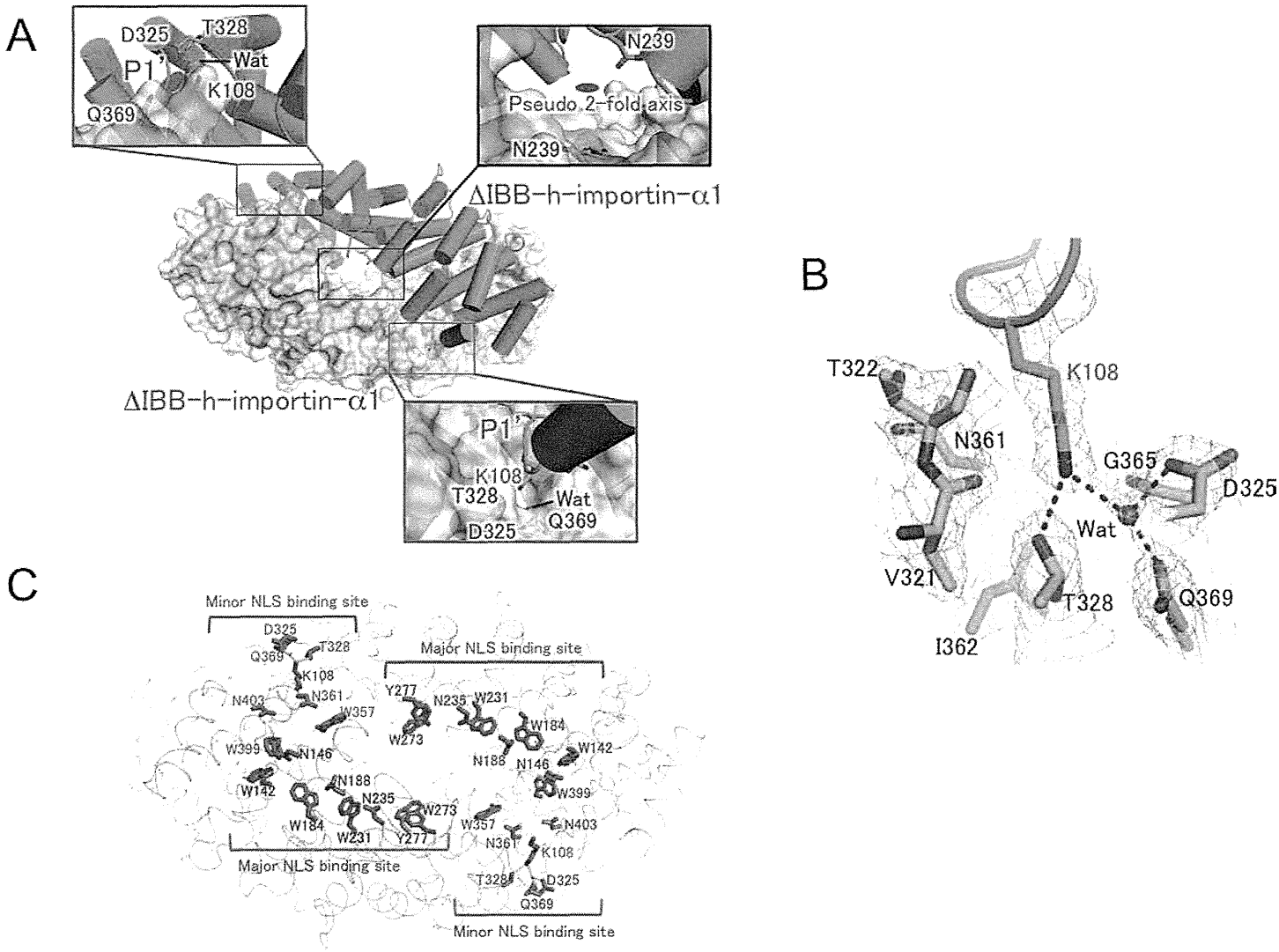

Fig 2. Crystal structure of homodimeric ΔIBB-h-importin-α1. (A) The closed homodimer structure of ΔIBB-h-importin-α1. One of the protomers is shown as a surface drawing. Both of the P1′-binding pockets are depicted in close-up views. The K108 inserts in the P1′-binding pocket, making hydrogen bonds with D325, T328, and Q369 of another protomer, and Wat (a water molecule). The pseudo 2-fold axis is drawn in the close-up view for the center of the dimer. (B) The P1′ binding pocket with 2fo-fc electron density maps (>1.0σ). Residues involved in the P1′-binding pocket are V321, T322, D325, T328, N361, I362, and Q369. One water molecule is depicted as Wat. The K108 of another protomer is inserted into the P1′-binding pocket, making hydrogen bonds depicted with dotted blue lines. (C) A ribbon drawing of the homodimeric ΔIBB-importin-α1 in cyan and gray. Residues of each protomer are in blue and orange. Major and minor NLS binding sites are indicated. Residues involved in the major NLS binding sites are W142, N146, W184, N188, W231, N235, W273, and Y277 in bold characters. The residues in the minor NLS biding sites are D325, T328, W357, N361, Q369, W399, and N403. Each of the K108 makes hydrogen bonds with D325, T328, Q369, and one water molecule in the minor NLS binding site of another protomer. Because the major and minor NLS binding sites are extensively buried in the dimerization interface as shown in the drawing, NLS signals are inaccessible to the sites. All molecular pictures were prepared with PyMol [40].

doi:10.1371/journal.pone.0115995.g002

B, which are in the disallowed region in the Ramachandran plot. Structural stress is probably put on them owing to the dimerization. The K108 residue is extensively involved in the dimer formation and is represented in the close-up views. The side chain of K108 enters the P1′ site of the minor NLS binding site [31], making hydrogen bonds with D325, T328, and Q369 of another protomer and one water molecule (Fig. 2B). The P1′ site comprises V321, T322, D325, T328, N361, I362, G365, and Q369, which are conserved in the minor NLS binding site of importin-α proteins (Fig. 3). The major (W142, N146, W184, N188, W231, N235, W273,

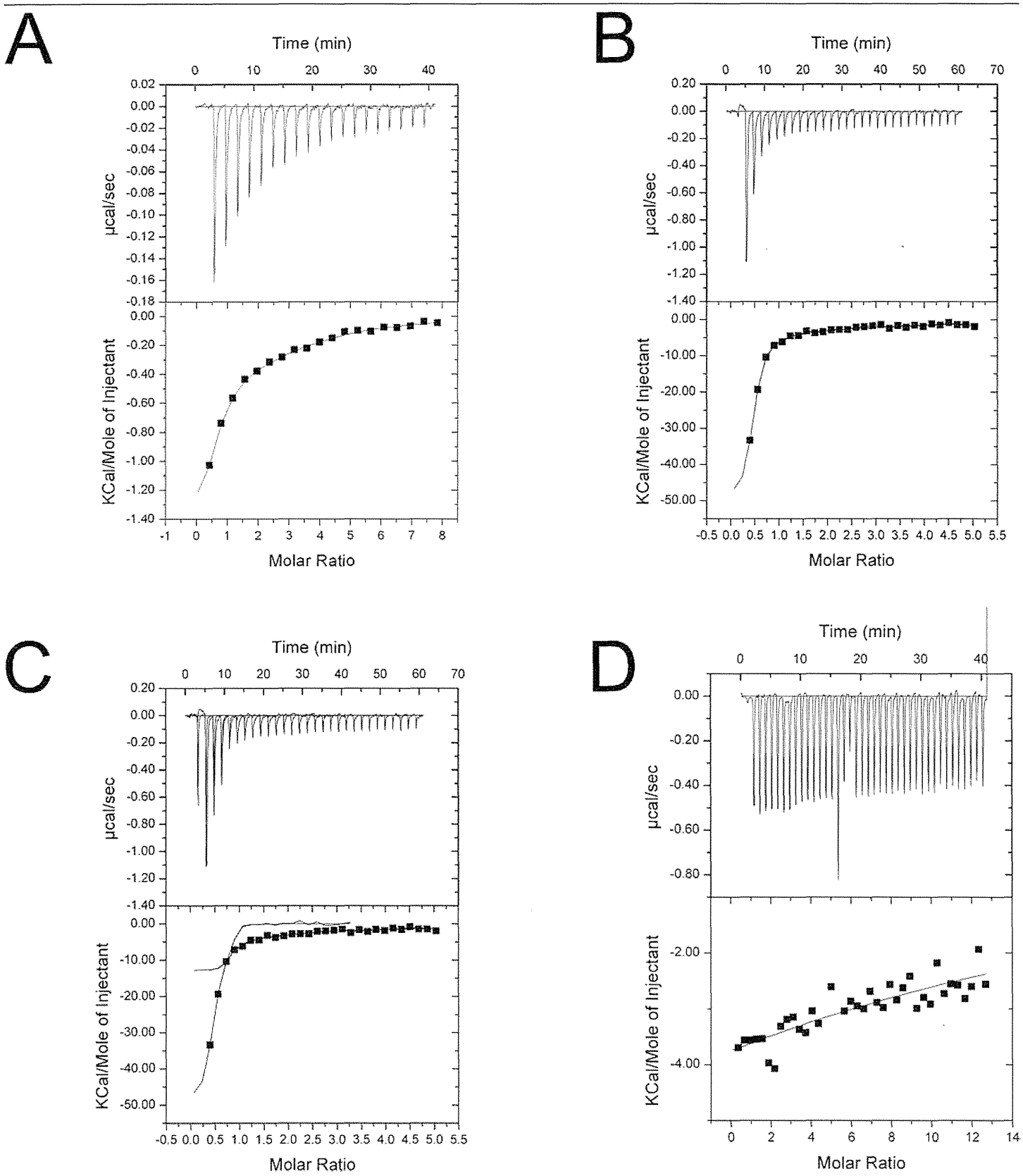

Fig 3. ITC fitting curves. (A) h-importin-α1 + SV40 NLS peptide. (B) ΔIBB-h-importin-α1 + SV40 NLS peptide. (C) ΔIBB-h-importin-α1 + nucleoplasmin NLS. (D) h-importin-α1 + nucleoplasmin.

doi:10.1371/journal.pone.0115995.g003

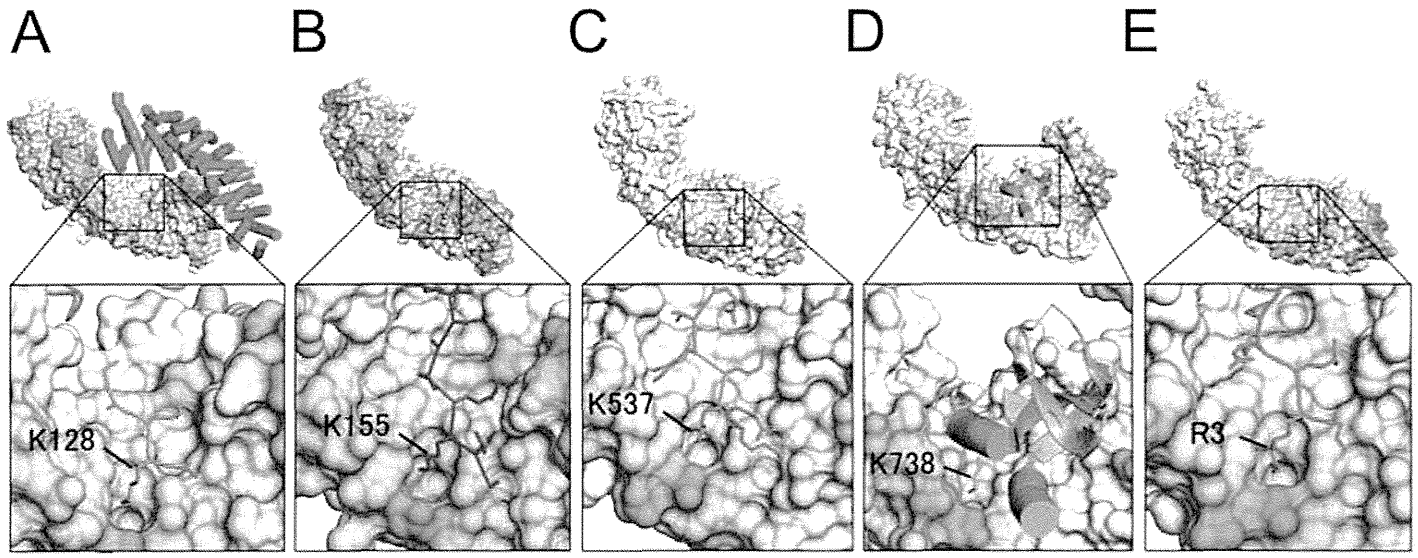

Fig 4. Crystal structures of complexes of importin-αs and NLS ligands with close-up views showing the P1′-binding pocket in the minor NLS binding sites. (A) K128 of SV40 NLS peptide (Yeast importin-α: PDB ID: 1BK6), (B) K155 of *Xenopus* nucleoplasmin NLS (Yeast importin-α: 1EE5), (C) K537 of *Xenopus* nucleoplasmin NLS (importin-α2: 1PJN), (D) K738 of influenza virus polymerase subunit Pb2 (importin-α5: 2JDQ), and (E) R3 of the IBB domain of the CBP20 (ΔIBB-importin-α1: 3FEY).

doi:10.1371/journal.pone.0115995.g004

Y277) and minor (W357, N361, W399, N403) NLS binding sites are buried in the dimer interface (Fig. 2C), thus NLS peptides cannot access the NLS binding sites. Because the major NLS binding site involves typically P1-P7 binding pockets [32], it has higher NLS binding affinity than the minor NLS binding site with P1′-P2′.

The P1′-binding pocket in the minor NLS binding site plays a common role in a variety of importin-αs; the P1′ accepts the K/R residues of the typical NLS signal motif KRXX [31–33], (Fig. 4). In the present crystal structure of ΔIBB-h-importin-α1, each of the K108 residues enters into the P1′-binding pocket of another protomer so that the minor NLS binding sites are in a state of autoinhibition (Fig. 2B), and, together with the major NLS binding sites, are buried in the dimer interface (Fig. 2C). As a result, the closed homodimer is stabilized owing to the limited access of NLS peptides to the major and minor NLS binding sites.

Isothermal titration calorimetry (ITC) assay for binding of NLS peptides to h-importin-α1 and ΔIBB-h-importin-α1

h-importin-α1. We carried out a binding assay of h-importin-α1 and ΔIBB-h-importin-α1 to study autoinhibition resulting from homodimerization. SV40 NLS bound to h-importin-α1 with a KD value of ~100 μM (Table 2). While the fitting to the ITC data, one-site binding model was used because two-site model did not converge to adequate values. The AUC-SV experiments reveal that h-importin-α1 is monomeric during SV40 NLS binding (Fig. 1G). This result suggests that both the IBB domain and the NLS peptides bind to the internal NLS binding sites and prevent homodimerization.

On the other hand, the bipartite nucleoplasmin NLS peptide did not bind to h-importin-α1 (Fig. 3D). This result suggests that NLS binding is restricted by the IBB domain.

Table 2. Binding parameters of h-importin-α1 and ΔIBB-h-importin-α1 by ITC.

Ligand: SV40 (PKKKRKV)			
Protein	**KD (μM)**	**N**	**ΔH (kcal/mol)**
h-importin-α1	102.1±11.0	0.8±0.2	-3.2± 0.9
ΔIBB-h-imporin-α1	5.5±2.0	0.5±0.1	-57.8±20.8
Ligand: Nucleoplasmin NLS (KRPAATKKAGQAKKKKK)			
Protein	KD (μM)	N	ΔH (kcal/mol)
h-importin-α1	N.D.		
ΔIBB-h-imporin-α1	0.14±0.05	0.8±0.0	-12.8±0.3

KD: dissociation constant,
N: number of binding sites,
ΔH: binding enthalpy,
N.D. not detectable.

doi:10.1371/journal.pone.0115995.t002

ΔIBB-h-importin-α1. ΔIBB-h-importin-α1 bound to SV40 NLS with KD = ~6 μM and to nucleoplasmin NLS peptides with KD = ~0.14 μM (Table 2). During the NLS binding, the monomer–dimer equilibrium shifted to the monomer side (Fig. 1D, E), which suggests that the NLS binding sites are involved in the dimer interface even in solution, as in the crystal structure.

Discussion

Homodimerization found in importin-αs

It has been shown or suggested that the importin-αs from yeast and *Xenopus* eggs form dimers. Yeast importin-α (PDB IB: 1BK6) provided the first crystal structure of an importin-α that was shown to dimerize not only in the crystal but also in solution, as revealed by dynamic light scattering (DLS) [13]. The SV40 NLS peptides are, however, able to bind to the NLS binding sites because the homodimer is an "open" structure where the NLS binding sites are exposed to the solution (Fig. 4A). The open homodimerization probably attributes to H119 at the top of the loop; this loop corresponds to the K108 loop of ΔIBB-importin-α1. H119 cannot enter the P1′-binding pocket in the minor NLS binding site, and this inability causes the protomers to slide along the long axis of the molecules. The NLS binding parameters of yeast importin-α were analyzed by fluorescence depolarization assay and it was found that yeast importin-α (1–542) binds to neither SV40 NLS-GFP nor Myc NLS-GFP [34]. On the other hand, yeast ΔIBB-importin-α (89–530) binds to both SV40 and Myc NLS, with KDs of 9 ± 4 nM and 6 ± 3 nM, respectively [35]. In addition, an enzyme-linked immunosorbent assay (ELISA)-based assay revealed that yeast importin-α (1–542) does not bind to SV40 NLS, whereas yeast ΔIBB-importin-α (88–530) binds very tightly [35]. These results suggest that the IBB domain is mainly responsible for the autoinhibition activity of yeast importin-α, while the "open homodimerization" does not restrict the NLS binding. Thus, the NLS binding affinity of yeast importin-α changes dramatically from 0% (off), when the IBB autoinhibits itself, to 100% (on), when it does not, that is keenly contrast to the closed-homodimer of h-importin-α1.

Moreover, it has been reported that wild importin-α from *Xenopus* eggs is homodimerized during purification [14], and a variety of studies have revealed that purified *Xenopus* importin-α is in dimer–monomer equilibration in the concentration range of 0.6~1.2 mM, with a